Spatial extent of the mid- to late Holocene sedimentary record of tsunamis along the Southern Kuril Trench, Hokkaido, Japan

Ryo Nakanishi[1,2], Juichiro Ashi[1,2], Yosuke Miyairi[1], and Yusuke Yokoyama[1,3,4,5,6]

[1]Atmosphere and Ocean Research Institute, The University of Tokyo, Kashiwa, 277-8564, Japan.

[2]Graduate School of Frontier Sciences, University of Tokyo, Kashiwa, 277-8561, Japan.

[3]Department of Earth and Planetary Sciences, Graduate School of Science, The University of Tokyo, Japan.

[4]Graduate Program on Environmental Science, Graduate School of Arts and Sciences, The University of Tokyo, Japan.

[5]Japan Agency for Marine-Earth Science and Technology (JAMSTEC), Japan.

[6]Research School of Physics, The Australian National University, Canberra, ACT0200, Australia.

Corresponding author: Ryo Nakanishi (n-ryo@g.ecc.u-tokyo.ac.jp)

Key Points:

- Geological surveys were conducted in southeastern Hokkaido, Japan to reveal tsunamis that originated in the Kuril Trench over 4000 years.
- The 17th-century sand layer was simulated as a tsunami by using the modified Mw~8.8 earthquake model.
- ^{14}C dating shows good agreement with the tsunami ages in the surrounding regions, suggesting that Kuril tsunamis have reached wider areas.

Abstract

Infrequent megathrust earthquakes, with their complex cycles and rupture modes, require a high-resolution spatiotemporal record of tsunami inundations over thousands of years to provide more accurate long-term forecasts. The geological record suggests that Mw>8 earthquakes in the Kuril Trench occurred at intervals of several hundred years. However, uncertainties remain regarding the rupture zone, owing to the limited survey areas and chronological data. Therefore, we investigated the tsunami deposits in a coastal wetland of southeastern Hokkaido, Japan, to characterize the tsunamis that have originated from the Kuril Trench over the last 4000 years. On the Erimo coast, more than seven sand layers exhibited the common features of tsunami deposits, such as sheet distributions of several hundred meters, normal grading structures, and sharp basal contacts. According to numerical tsunami simulations, the 17th-century sand layer could be reproduced by using a multiple rupture zone model (Mw~8.8). We used high-resolution radiocarbon dating and tephras to correlate the tsunami deposits from the last 4000 years with those reported from regions ~100 km away. The tsunami history revealed here shows good agreement with histories of adjacent regions. However, the paleotsunamis reported to have occurred in regions > 200 km away include some events that differ from those in this study, which suggests a diversity of Mw>8 earthquakes in the Kuril Trench. We clarified the history and extents of earthquake-generated tsunamis along the southwestern end of the Kuril Trench, which were previously unknown. Our results provide a framework for magnitude estimations and long-term forecast of earthquakes.

Keywords: Tsunami deposits, Kuril Trench, Radiocarbon dating, Numerical simulation, Hokkaido, Erimo

Plain Language Summaries

Long-term assessments of infrequent large earthquakes and tsunamis are highly uncertain due to the complexity of their cycles and rupture zone. Unveiling the nature of past tsunamis is critical for understanding the complex mechanisms of megathrust earthquakes. However, the period of time covered by observational data is often insufficient to characterize infrequent events. High-resolution spatiotemporal records of coastal inundation caused by tsunamis over thousands of years are therefore required to constrain geophysical models. In this study, we performed geological surveys along the southeastern coast of Hokkaido, Japan. Ten tsunami-derived sand layers were newly observed. According to numerical simulations, the 17th century sand layer could be reproduced by a tsunami from the earthquake model in the Kuril Trench. The tsunami history is well matched with that of the surrounding region facing the Kuril Trench. However, some layers did not correlate with sand layers in in regions > 200 km away, suggesting that another process produced these sand layers. We found that some of the earthquakes categorized as "unusually large earthquakes" included multiple ruptures, and the spatial distribution of sand layers suggests localized or differing rupture modes from that of the 17^{th} century event.

1 Introduction

Infrequent megathrust earthquakes (M~9: e.g., the 1700 Cascadia, 1960 Chile, 2004 Sumatra, and 2011 Tohoku-oki earthquakes) have been reported to occur over wider rupture zones and with prolonged recurrence intervals of hundreds to thousands of years compared to M7–8 earthquakes (Sieh et al., 2008; Goldfinger et al., 2013; Philibosian & Meltzner, 2020; Salditch et al., 2020). To study these infrequency megathrust earthquakes, prehistoric data with timescales ranging from thousands to tens of thousands of years are required. Prehistoric data can be obtained only from the geological record. For instance, these data can be obtained from uplifted terraces, deep-sea turbidites, and tsunami deposits (Goldfinger et al., 2013; Satake, 2015; Hutchinson & Clague, 2017). Every subduction zone has a high danger of M~9 earthquake recurrence because the instrumentally recorded earthquakes do not completely relieve the strain in such zones. Therefore, it is necessary to investigate the case studies of infrequency megathrust earthquakes from various regions as event clusters, and the changes in rupture zone patterns differ for each subduction zone (Nelson et al., 2006; Philibosian & Meltzner, 2020; Salditch et al., 2020).

The geological evidence provided by tsunami deposits and seismic crustal deformation along the Pacific coast of eastern Hokkaido indicates that the southern Kuril Trench has repeatedly ruptured at intervals of several hundred years, with the most recent event occurring in the 17th century (Nanayama et al., 2003; Sawai et al., 2004, 2009; Kelsey et al., 2006; Sawai, 2020). Based on the evidence provided by the tsunami deposits from the 17th century, which have been found at many sites in eastern Hokkaido, it is suggested that this earthquake was Mw 8.8 or greater based on the numerical tsunami simulations of (Nanayama et al., 2003; Ioki & Tanioka, 2016). Therefore, another rupture is expected to occur in the near future, as ~400 years have passed since the 17th-century earthquake (Sawai, 2020). It is necessary to clarify the detailed magnitudes of Mw>8 earthquakes via geological surveys over wide areas since there are limited historical documents regarding the paleotsunamis in Hokkaido. More than 17 sand layers have been reported to have been deposited over several thousand years in east Hokkaido (Nanayama et al., 2003; Sawai et al., 2009: Fig. 1). Some of these sand layers were deposited by "unusually large" earthquake-generated tsunamis, such as the 17th-century tsunamis, which could not be explained by the observed historic tsunamis. For events that took place prior to the 17th century, chronological correlations have rarely been examined, but accurate correlations of these tsunami records are important for understanding the recurrence intervals and rupture modes of megathrust earthquakes.

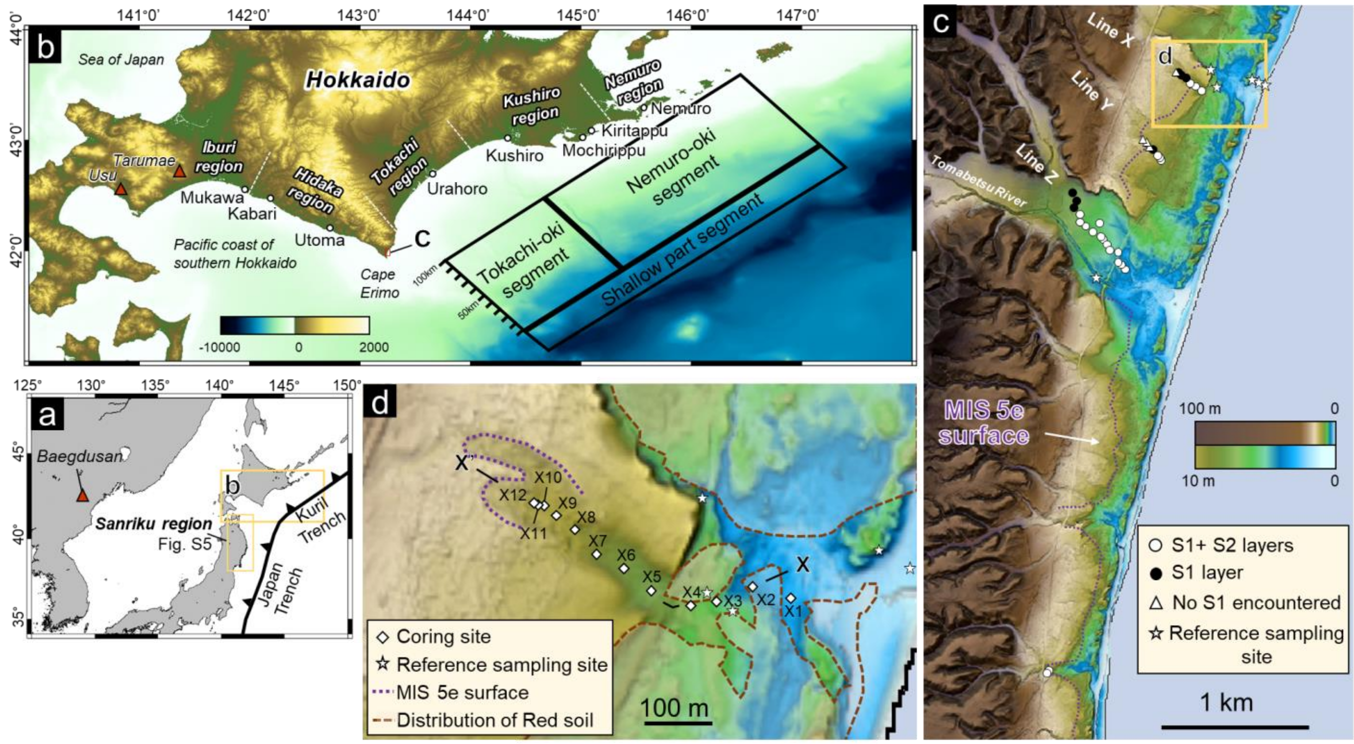

Figure 1. Study area. a: Location map of Hokkaido and Baegdusan. The black barbed line indicates the Pacific Plate subduction zone. b: Bathymetric and topographic map of Hokkaido. The paleotsunami investigation sites and local sources of tephra described by Nakanishi et al. (2020b) are marked. The black boxes indicate the area of the 17th-century earthquake fault model (Ioki & Tanioka, 2016). c: Topographic map based on 5 m-grid digital elevation model data from the Erimo area. The circles and triangles indicate the locations of coring sites. Additionally, the circles show the distributions of layers S1 and S2. The purple dashed lines indicate the distribution of the MIS 5e surface (Koike & Machida, 2001). The stars show the sand sampling locations for beaches, rivers, and Red soil. The yellow box indicates the map shown in Fig. 1d. d: Close-up map of the coring sites that are located along Line X. The distribution of Red soil in 1947 is shown, as interpreted from aerial photographs. The stars are the same as in Fig. 1c.

In this study, we investigated the eastern coast of Cape Erimo to identify tsunami deposits and to estimate their spatial distributions and to also estimate the wave sources of the 17th-century tsunami deposits that were newly discovered in this area by using numerical simulations. The tsunami deposits are correlated with the event layers in the surrounding regions where the event ages have already been reported based on ^{14}C dating and tephrochronology. This study discusses the tsunami history and coastal extents over the last 4,000 years along the Kuril Trench from the Tokachi to Hidaka region based on tsunami age correlations.

2 Background

2.1 Historical tsunami records

Instrumentally recorded earthquakes over the past 200 years in the southern part of the Kuril subduction zone are known to occur at magnitudes of Mw 7–8 and fault lengths of ~100 km with maximum lengths of 200 km (Satake, 2015). The rupture zone is classified into two segments, Tokachi-oki and Nemuro-oki (Fig. 1). Interseismic GPS data and seismic wave velocity studies suggest a gap in the asperity distributions in these rupture zones (Hashimoto et al., 2009; Liu et al., 2013). Mw 7–8 earthquakes are known to occur at intervals of 50–100 years, with the Tokachi-oki or Nemuro-oki segments acting as rupture faults (Satake, 2015; Sawai, 2020). The most recent southern Kuril Trench earthquake to cause significant damage was the 2003 Tokachi-oki earthquake (Mw 8.0), which generated a tsunami with a maximum wave heights of 4 m (Tanioka et al., 2004). This tsunami caused traces debris deposition and minimal erosion of up to 3.5 m above present sea level (asl) in the Erimo area of Hokkaido, however, no sandy deposits were formed (Nishimura et al., 2004). Earlier historical tsunamis originating from the Kuril and Japan trenches generated wave heights ranging as 3–4 m along the Erimo coast. However, no significant sandy deposits were created by these tsunamis (Nakanishi et al., 2020a).

2.2 Previous work on geological records of tsunami

There are no historical records for Hokkaido before the 19th century (Satake, 2015), but geological investigations of the tsunami deposits and seismic crustal deformations have been reported (Nanayama et al., 2003; Sawai et al., 2004, 2009; Kelsey et al., 2006; Szczuciński et al., 2016; Ishizawa et al., 2017; Nakanishi et al., 2020a). In the region from Tokachi to Nemuro, extensive surveys of tsunami deposits have been carried out (Nanayama et al., 2003). Based on tephrostratigraphic correlations, previous studies have identified two sand layers that were deposited between the 17th and 10th centuries, and 2–4 sand layers were identified to have formed between 1000 and 2400 years ago. These tsunami deposits have anomalous distribution heights and extents that cannot be reproduced by tsunamis that were generated by Mw~8 earthquakes, such as the 1952 and 2003 Tokachi-oki earthquakes (Nanayama et al., 2003, 2007; Sawai et al., 2009). These data suggest that these deposits were caused by tsunamis that were generated by Mw~9 earthquakes that occurred in the rupture zones along the Tokachi-oki and Nemuro-oki segments. However, detailed correlations among these sand layers are unclear due to a lack of comprehensive radiocarbon data (Sawai, 2020). The tsunami history of Kushiro to Nemuro regions has been investigated based on widespread tephra and radiocarbon dating of tsunami deposits for the past 7,000 years (Nanayama et al., 2003, 2007; Sawai et al., 2009). However, the age comparisons of these regions are difficult because of the large errors in the obtained ^{14}C ages. Precise radiocarbon dating has been reported for the tsunami deposits over the past 3000 years in the Urahoro, Tokachi region (Ishizawa et al., 2017), which is located ~100 km from Erimo (Fig. 1).

2.3 Regional setting

The eastern coast of Cape Erimo is located at the southern end of the Hidaka region and faces the Tokachi-oki segment (Fig. 1). This coastal area contains an ~200 m wide sandy beach where the maximum dune height is ~10 m asl. The first recorded settlement with a large number of immigrants was in 1872. Desertification of the area progressed owing to deforestation until a greening project was initiated in 1953 (Sakuraba, 2019). Aerial photographs taken in 1947 show that the coast was originally covered with aeolian redeposited volcanic ash material called "Red soil", which extended over 500 m perpendicular to the coastline (Fig. 1d). The seafloor sediments on the eastern side of Cape Erimo consist of poorly sorted very fine- to fine-grained sand (Noda & Katayama, 2011). Glauconite grains and sessile organisms were found east of Cape Erimo (Noda & TuZino, 2010).

Terrace surfaces of marine isotope stage (MIS) 5e are widely distributed in this area (Fig. 1c), and relative sea-level change can be inferred from this elevation. Based on glacio-hydro isostatic adjustment (GIA) models, the relative sea-level change due to the GIA over the past 6000 years in the Erimo area was estimated to be 0 ± 1 m (Okuno et al., 2014). Marine terraces during MIS 5e extend parallel to the coast at ~15–25 m asl (Koike and Machida, 2001). The uplift rate is 0.02–0.17 mm/yr based on the MIS 5e terraces on the Erimo coast, when GIA estimations of 125 ka are considered (Okuno et al., 2014). The Erimo coast consists of a microtidal area where the maximum tidal range is < 1 m and the difference between mean sea level and mean higher high water is ~0.4 m (J-DOSS: https://www.jodc.go.jp/jodcweb/JDOSS/index.html).

We surveyed the wetlands along three survey lines (Fig. 1). Lines X and Y traverse the depressions on the marine terraces. A depression oriented perpendicular to the coastline on the marine terrace is considered to be a former riverbed, which is flat near the terrace surface of MIS 5e, suggesting that the rivers ceased to flow before at least 125 ka. Line Z is parallel to the Tomabetsu River, and this area is covered by a thick peat layer. The inland area was not surveyed owing to the construction of residential areas.

3 Methods

3.1 Field surveys

Core samples were obtained from three survey lines (40 sites) to investigate the spatial distribution of the tsunami deposits, especially those that were laid down after the 10th century. The samples were extracted using a handy Geoslicer (length of 0.6 m: Takada et al., 2002) and peat sampler (diameter of 7 cm, length of 2.5 m). We sampled the pre-10th-century sediments based on the B-Tm tephra layer to depths of 1–2.5 m to investigate the changes in the sand layers in the inland direction along Line X. The variation of layer thickness was confirmed to be as small as 1 cm from the average value by the repeat hand-boring check at several sites (Table S1). The core samples were described by their sedimentary facies (e.g., colors, grain sizes, thicknesses, bedforms) and were photographed. Thereafter, the whole cores were placed in plastic cases and were subsampled in the laboratory for each laboratory analysis. Beach, river, and aeolian sand (Red soil) samples around the peatland were collected to examine the sources of the sand layers (Fig. 1). The elevation profile along survey Line X was measured via real-time kinematic positioning using multiband global navigation satellite system receivers (GNSS: ZED-F9P U-blox). The data pertaining to forests, where the signal reception was not consistent, were supplemented by correcting the Digital Elevation Model (DEM: https://fgd.gsi.go.jp/download/menu.php) data of the Geographical Survey Institute (GSI) to ensure data matching with respect to the GNSS data.

3.2 X-ray diffraction analysis

Since the mineral combinations of the deposits may reflect the sediment sources as well the sedimentation conditions (Jagodziński et al., 2012; Nakamura et al., 2012), X-ray diffractometry (XRD) analyses were conducted to study the mineralogy of the sand layers. Twenty-three sand and mud samples were collected from the core samples, and the candidate source sand samples. The sand samples were sieved to separate the 0.18–0.25 mm fraction. We also analyzed the 0.090–0.063 mm fraction of the sand samples to determine the grain size effects. The mineralogical compositions were determined by XRD (Bruker D2 PHASER) and were determined by the same method described in Nakanishi et al. (2020a). The analysis conditions were set at 30 kV, 10 mA, 0.02 steps for 1 s, and a 2θ registration range from 5° to 65°.

3.3 Grain size analysis

The grain size distributions of sand layers are widely used to determine their origins and transport modes (e.g., Folk & Ward, 1957; Morton et al., 2007). We performed grain size analyses by using the sieve method on the sand layers that were obtained from the cores and the surrounding sands (e.g., beach, river, and aeolian sands). We sampled 47 samples in total, which were obtained every 1 cm in the vertical direction at site X5 and from the bulk layers at other sites. Samples of 10–20 g were pretreated with H_2O_2 to remove the organic matter and disperse the particles. The dried samples were sieved by using a set of 14 sieves with mesh sizes ranging from 4.5 phi to -2.0 phi. The basic statistics such as the mean (Mz), standard deviation (σ_I), and skewness (Sk_I) were calculated by following the method outlined in Folk & Ward (1957).

3.4 Computed tomography (CT) and magnetic susceptibility analysis

X-ray CT image scanning was performed to confirm invisible sedimentary structures of the core samples due to density differences. Analysis was performed with a slice width of 0.5 mm using an Aquilion PRIME Focus Edition (Canon Medical Systems Corporation) at the Kochi Core Center.

Magnetic susceptibility measurements were performed to characterize the sediments and to identify magnetite. Cores sampled in plastic cases were kept at room temperature and then measured every 1 cm using an MS3 susceptometer (Bartington Instruments) and a susceptibility accuracy of $\pm 2 \times 10^{-6}$ SI. We corrected for atmospheric conditions per 10 measurements.

3.5 Diatom analysis

Diatom fossils transported with sand layers have information about the source, as some diatoms have specific habitats. Samples were taken from pure sand layers that were not muddy and peat layers below sand layers. The sand layers were sampled from the middle of the sand layer to avoid the inclusion of peat materials such as rip-up clasts. Optical microscopic observations were performed in following Nakanishi et al. (2022a). In total, 200 diatom valves were counted and, expressed as percentages; species or genera present by > 3% were used for assemblages analysis.

3.6 Radiocarbon dating

Radiocarbon dating was used to determine the depositional ages of the tsunami deposits (Table 1). Analytical samples (units of 1 cm) were collected above and below the sand layers and consisted of plant fragments in peat while avoiding roots. When plant fragments were not available, bulk samples were used for the measurements. Graphitization of the samples was achieved via the same method employed by Nakanishi et al. (2020a), and ^{14}C dating was prepared at the Atmosphere and Ocean Research Institute using single-stage accelerator mass spectrometry (Yokoyama et al., 2019). We calibrated the ^{14}C ages to the calendar ages using OxCal 4.4 with the IntCal20 dataset (Reimer et al., 2020). The P_Sequence and Sequence model and general outlier model in OxCal were used to constrain the calibration ages by using the stratigraphic order (Bronk Ramsey, 2008, 2009a, 2009b). Each model was constructed separately for individual peat layers that were located among the tsunami deposits (Ishizawa et al., 2017, 2020). The tsunami recurrence intervals were estimated from the age differences between each sand layer (Lienkaemper & Bronk Ramsey, 2009: Table S2). We recalibrated the ^{14}C ages of the reported tsunami deposits (Ishizawa et al., 2017; Nakanishi et al., 2020a) using updated IntCal20 (Reimer et al., 2020).

Table 1. ^{14}C dating results.

Sample name	Site	Depth (cm)	Material	^{14}C age	Error	Modelled age (1σ) from	Modelled age (1σ) to	Modelled age (2σ) from	Modelled age (2σ) to	Mean	Lab number
S1_2U	X5	-30	Bulk peat	392	±25	500	461	511	335	469	YAUT-053023
S1_2L		-35	Bulk peat	814	±24	714	683	733	677	702	YAUT-053019
S2L		-41	Bulk peat	862	±22	776	732	897	725	766	YAUT-053018
S5U		-54	Bulk peat	1475	±24	1379	1315	1393	1307	1352	YAUT-053017
S5_6U		-60	Bulk peat	1801	±26	1728	1630	1780	1608	1684	YAUT-053016
S5_6L		-66	Bulk peat	1971	±24	1925	1838	1977	1827	1888	YAUT-053015
S6_7U		-70	Bulk peat	2053	±27	2051	1950	2098	1940	2012	YAUT-053013
S6_7L		-71	Bulk peat	2119	±23	2120	2048	2145	2004	2082	YAUT-053012
S7L		-78	Plant fragment	2304	±25	2350	2324	2358	2182	2322	YAUT-053011
S8U		-83	Plant fragment	2524	±23	2719	2515	2732	2492	2587	YAUT-053009
S8_9U		-100	Plant fragment	2679	±24	2841	2755	2850	2750	2792	YAUT-053006
S8_9L		-106	Plant fragment	3010	±26	3240	3156	3331	3075	3198	YAUT-053005
S9_10U		-112	Plant fragment	3216	±25	3460	3401	3480	3379	3428	YAUT-053004
S9_10L		-115	Plant fragment	3411	±24	3672	3578	3703	3568	3631	YAUT-053003
S10L		-121	Plant fragment	3563	±25	3897	3833	3969	3728	3863	YAUT-053002

Sample name	Site	Depth (cm)	Material	^{14}C age	Error	Calibrated age (1σ) from	Calibrated age (1σ) to	Calibrated age (2σ) from	Calibrated age (2σ) to	Mean	Lab number
X4_195cm	X4	-195	Plant fragment	3628	25	3976	3900	4071	3849	3942	YAUT-053024

The calibrated ages are reported in solar years before 1950 CE.

Analytical Laboratory: Atmosphere and Ocean Research Institute, the University of Tokyo.

Half-life of ^{14}C is 5730 year.

3.6 Numerical simulation

We performed numerical simulation to reproduce the sand layers in this area by assuming tsunami inundation that is consistent with the observed distribution of tsunami deposits in eastern Hokkaido using the source faults of the 17th-century earthquake (Satake et al., 2008; Ioki & Tanioka, 2016). If the model was inconsistent, the fault parameters were modified for optimization. The numerical simulations were performed using the tsunami calculation code "JAGRUS" (Baba et al., 2015, 2017). We used bathymetric data obtained from the Japan Oceanographic Data Center and M7000 series data obtained from the Japan Hydrographic Association. The ASTER GDEM Version 3 from the Shuttle Radar Topography Mission (https://doi.org/10.5067/ASTER/ASTGTM.003) and 5-m mesh DEM data from the GSI were used as topographical data. To avoid underestimating the inundation area, modern roads that are assumed to have not existed in the 17th century were manually removed and flattened using the surface command of the generic mapping tools (Wessel et al., 2013). We nested the geographical data in grid size in the following order: 450, 150, 50, 16, and 5 m. The calculations were performed using linear long-wave equations for the 450 m grid size system and non-linear long-wave equations for the finer grid size systems in a staggered-grid, leap-frog finite differential scheme. The absorbing boundary condition was applied at the edge of the computational domain. The time step was 0.1 s to safely reach a stabe condition. The values of Manning's roughness coefficient was 0.03 $m^{-1/3}s$, based on Ioki & Tanioka (2016). The tide levels were assumed to be constant at the present mean sea level. Seismic deformations were computed based on the formula of Okada (1985), and the rise times were assumed to be 60 s (deformation was included in the geographical data). The tsunami propagation calculations were conducted for as long as 7200 s.

4 Description of tsunami deposits

4.1 Stratigraphy and depositional ages

An outline of the stratigraphy on the survey lines observed by hand borings is described in Fig. 2. From bottom to top: fibrous dark brown peat or clay layer, black peat intercalated by gray sand layers, reddish-brown soil or sand as "Red soil", and topsoil. On the landward side of the X6 site, the clay layer consists of pinkish-brown to yellowish-brown sticky clay at depths of ~0.5 m or more from the ground surface (Figs. 2 and Fig. S1). On the seaward side of the X5 site, a fibrous peat layer was observed below ~1.5 m from the ground surface. Here, the sand layers were either thinner than 5 cm thick, or no sand layers were observed.

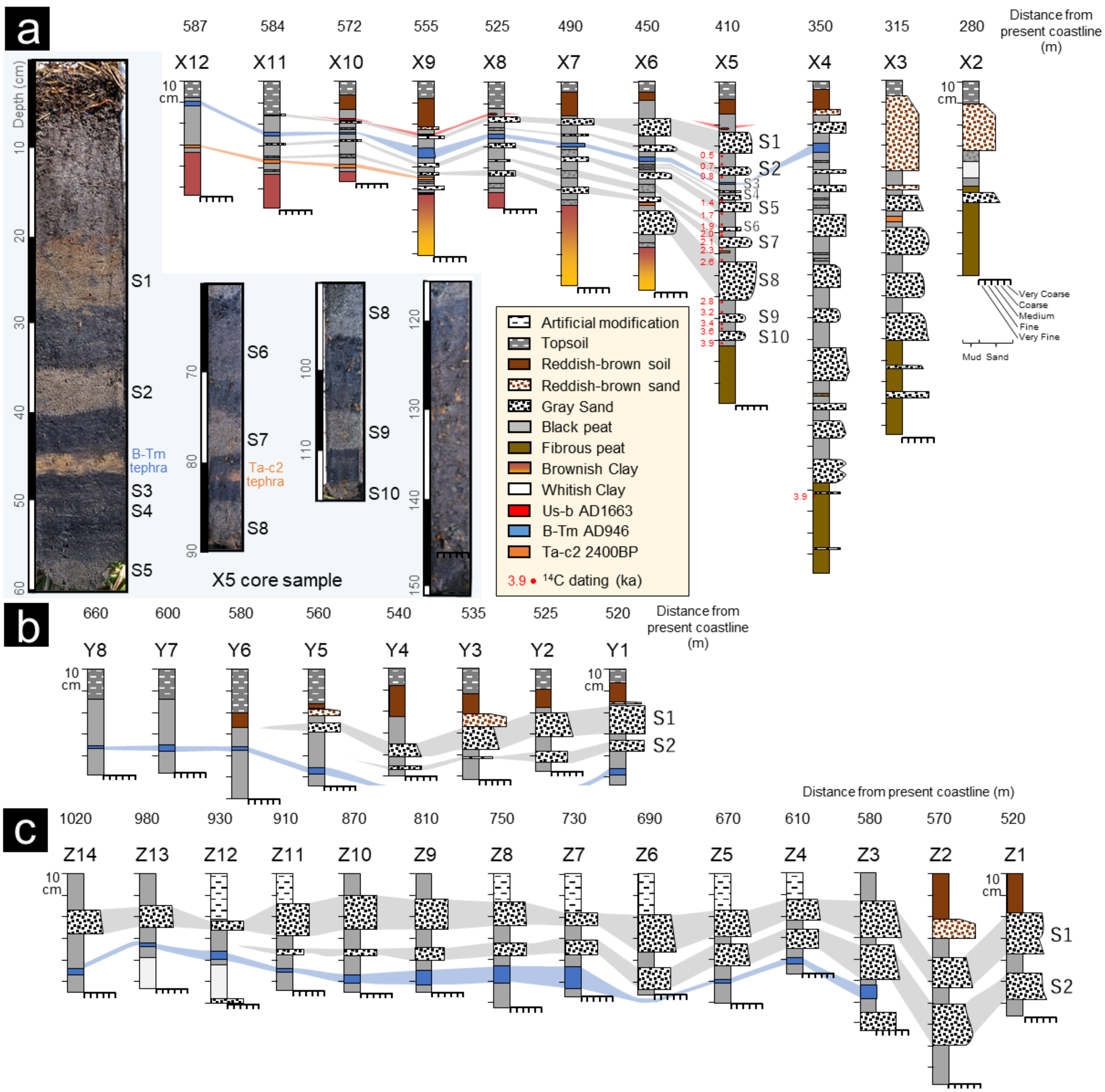

Figure 2. Correlated stratigraphic columns along survey Line X, Y, and Z and photographs of the core samples from site X5.

Three tephra layers and ten sand layers were intercalated within the black peat (Fig. 2). The tephra layers were identified in this area by Nakanishi et al. (2020b), and from top to bottom consist of: a patchy white volcanic ash layer (1663 AD, Usu Volcano-b tephra: Us-b), a yellowish-white volcanic ash layer with a thickness of ~2 cm (946 AD, Baegdusan Volcano-Tomakomai tephra: B-Tm), and an orange volcanic ash layer with patchy 2-cm thickness within the peat layers (~2400 BP, Tarumae Volcano-c2 tephra: Ta-c2). The chemical compositions of their volcanic glasses differ, reflecting the different source volcanoes (Fig. S2). Us-b is characterized by the presence of hornblende, mainly volcanic glasses. The distribution is discontinuous owing to the thin thickness and its disturbance by the Red soil layer. B-Tm is particularly easy to identify because it is composed of > 90% volcanic glass. The Ta-c2 layer is characterized by high magnetic susceptibility due to a high magnetite content (Fig. 3).

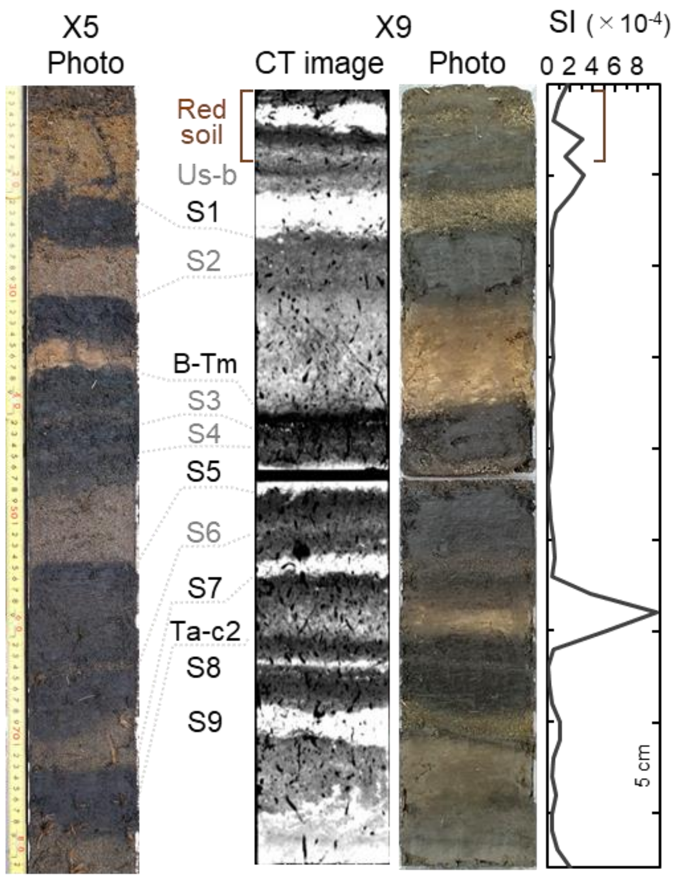

Figure 3. Computed tomograhy (CT) image and magnetic susceptibility of the X9 core. Gray letters show invisible sand layers identified in the CT image. A photograph of the X5 core is shown for comparison.

We observed two sand layers between the Us-b and B-Tm tephras, five sand layers between the B-Tm and Ta-c2 tephras, and three to five sand layers below the Ta-c2 tephra (named layers S1–10 from top to bottom). In the age–depth model, the depositional ages were obtained from the peat layers by ^{14}C dating and the tephras were linearly correlated (Fig. 4). This model is also consistent with the known ages of the volcanic ash layers. The accumulation rate was constant (0.14 mm/yr), which indicated continuous deposition of the peat layers. The most basal sand layer (i.e., layer S10) was deposited after 3900 BP. The recurrence intervals for layers S1–10 ranged from 110 to 620 years (Table S2).

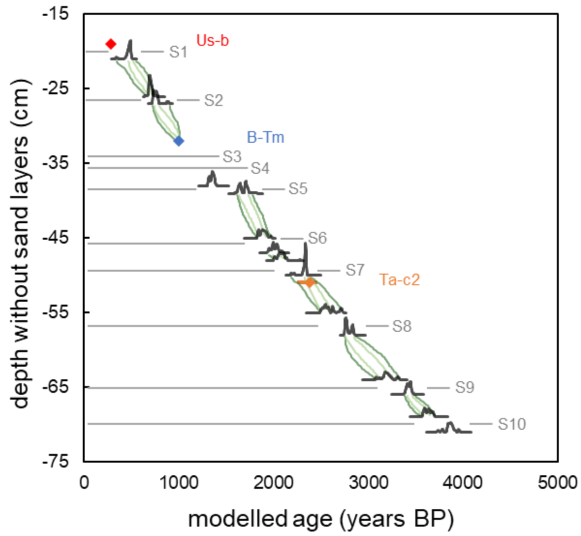

Figure 4. Age-depth model without the sand layers at site X5. Black histograms show the modeled ^{14}C ages (Table 1). The dark and light green lines indicate the ranges of the 2σ and 1σ modeled ages, respectively. Red and blue diamonds indicate the widespread tephras (e.g., Us-b: 1663 AD, B-Tm: 946 AD) that were incorporated into the age-depth model. Yellow diamonds and bars indicate the Ta-c2 median ages and 2σ ranges that were calculated by the same methods as used for the event layers, respectively. The calibrated ages are reported in solar years before 1950 CE.

A reddish-brown sand layer and soil were found as “Red soil” near the ground surface. The reddish-brown sand layer has a mode of 1.5 phi with poor sorting and a high background and low mineral peak XRD intensity (Figs. 5 and 6, Figs, S3 and S4), which indicates high levels of amorphous components such as a pumice. The magnetic susceptibility is higher than that of peats and gray sand layers because of its volcanic ash origin (Fig. 3). Therefore, the reddish-brown sand layers can be distinguished from the gray sand layers by their distributions near the ground surface and poor sorting. The topsoil is black to dark brown, but the boundary with the Red soil is unclear.

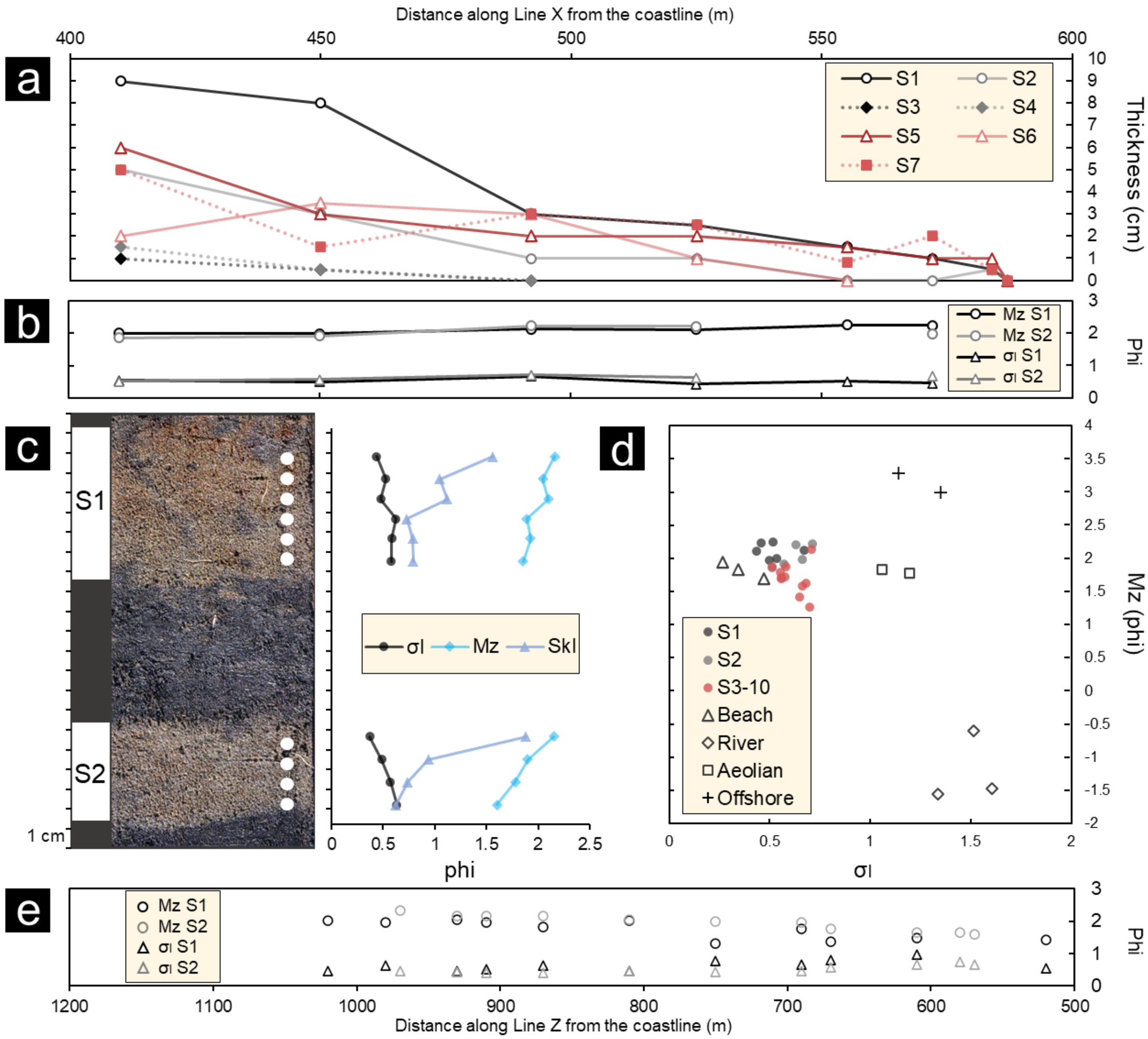

Figure 5. Layer thickness and grain size analysis results for the sand layers and candidate source sands. a: Layer thickness changes of layers S1–7 on Line X. b: Horizontal changes in the mean diameters (Mz) and standard deviations (σ_I) of layers S1 and S2 on Line X. c: Vertical changes in the mean diameters, standard deviations, and skewness values (Sk_I) for layers S1 and S2. d: Scatter plot of the mean diameters and standard deviations in layers S1–10 on Line X, beach, river, aeolian (red soil), offshore sand. The offshore grain size

composition data are from Noda & Katayama (2011). e: Horizontal changes in the mean diameters standard deviations of layers S1 and S2 on Line Z.

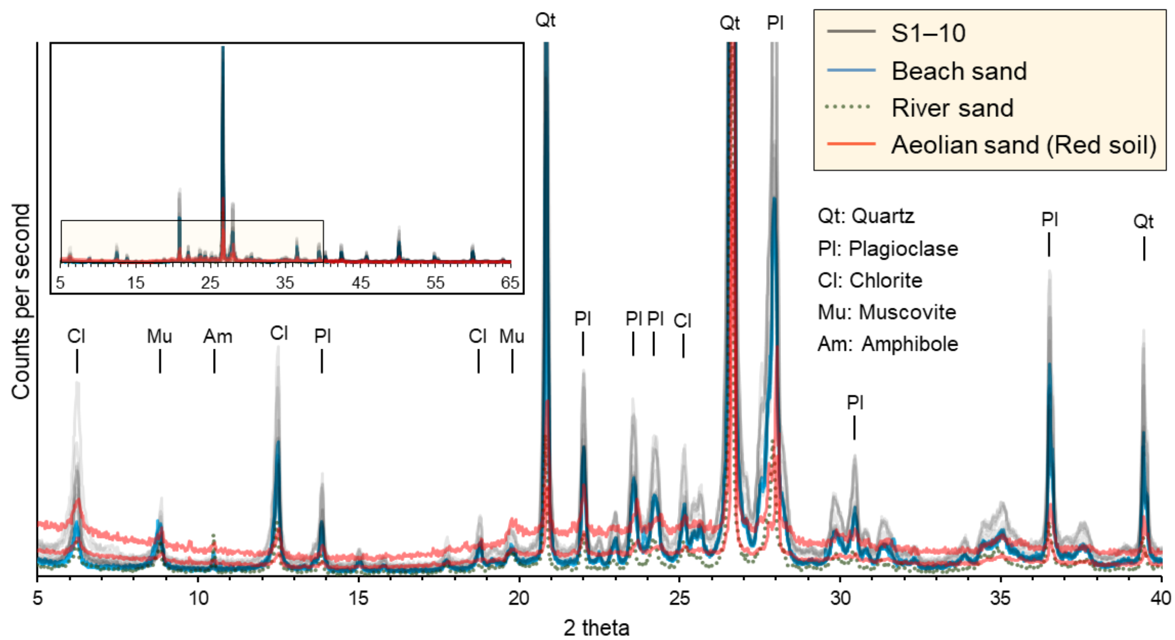

Figure 6. Results of mineralogy analysis using XRD for layers S1–10 at site X5 (10 samples), beach sand (3 samples), river sand (1 sample) and Red soil (2 samples). The figures show the full view and the zoomed-out part. Each abbreviation indicates Am: Amphibole, Cl: Chlorite, Mu: Muscovite, Pl: Plagioclase, Qt: Quartz.

4.2 Sand layer features

The S1–10 layers consist of well- to moderately well-sorted fine to medium sands (Fig. 5). These sand layers commonly exhibit single normal grading and sharp basal contacts. Some of the thick sand layers contained rip-up clasts of black peat (Fig. S1). The S1–8 layers exhibited modes of 2.5 phi and demonstrated very positive skewness. The grain size compositions of layers S9 and S10 consisted of 0.5–2.5 phi and moderately well sorted sand along X5 (Fig. S3). The mineral assemblages of layers S1–10 mainly consisted of quartz, feldspar, and chlorite, with low background values, which indicated few amorphous components (Fig. 6). The mineral assemblages do not vary significantly with the sample grain sizes or distances from the coastline. The mineral assemblages of the beach and river sands are similar to those of layers S1–10, but the river sands differ from layers S1–10 in that they have higher proportions of amphibole and lower proportions of other minerals.

Diatom assemblages in the peat and overlying sand layers are very similar, but the sand layers contained brackish and marine species (Fig. 7). The diatom assemblages in the peat layers are dominated by freshwater benthic or aerophilic species such as Pinnularia, Caloneis, Rhopalodia, and Diploneis genera. In addition to these species, the sand layer contains different habitat species such as Placoneis elginensis (Chiba & Sawai, 2014), an indicator species for swampy wetlands, and epontic Gomphonema genera. In addition, the site is characterized by the presence of a few species that are known to inhabit tidal flats and the open sea.

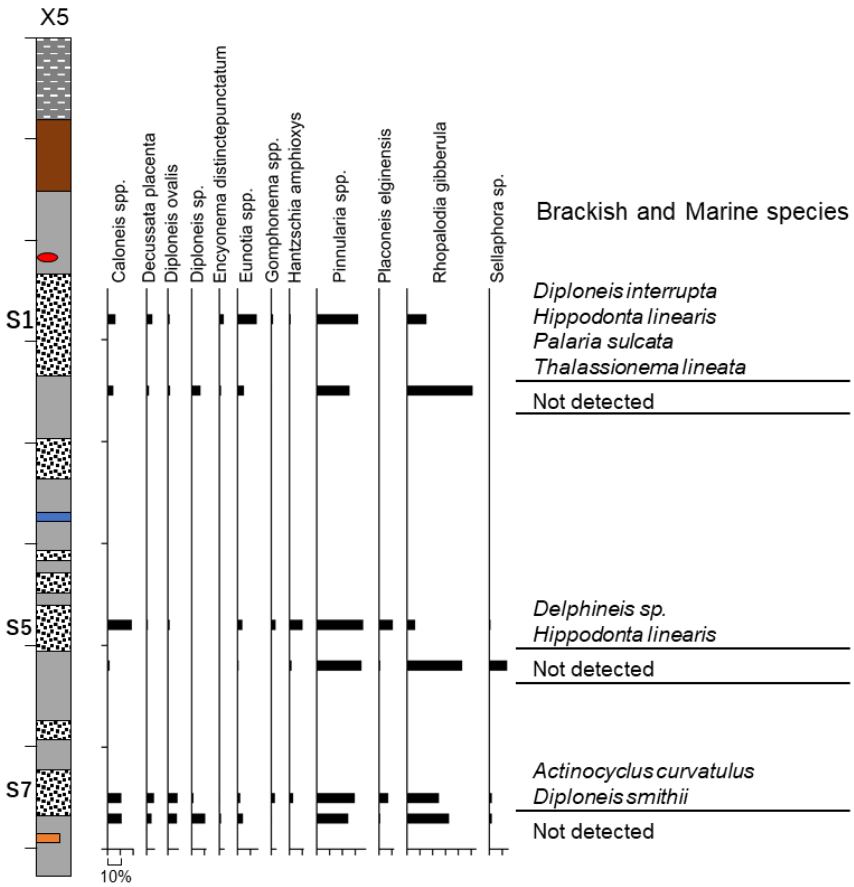

Figure 7. Results of diatom analysis on the sand layers and the below peat layers at X5. A list of brackish and marine species found in the analyzed samples is shown.

Correlations among the cores were estimated based on the tephras and the thicknesses of the peat layers. The peat layer up to the Red soil is homogeneous and stable with very little clastic detritus; moreover, it has very low density, as indicated by the CT image (Fig. 3). In addition, there is a gradation of density in the peat above the fine volcanic ash layers, while the boundary is clear above the sand layers. Diatom assemblages supported a calm environment where no running water was involved, as benthic species were dominant, and diversity was low (Fig. 7). The sand layers inland from X9 are thin and shows slight normal grading of a few centimeters, which suggests that these sediments were transported by suspension and deposited without significant erosion. Moreover, the black peat layer exhibited a constant accumulation rate, as shown by the age–depth model (Fig. 4). Therefore, peat thickness was assumed to be proportional to the duration of the accumulation period. The S1–S7 layers are visible between Us-b and Ta-c2 until X6, but at X9, only three sand layers were visible (Fig. 2). However, the

CT image of the X9 core shows sand layers invisible by naked eye, corresponding to layers S2, S3, S4, and S6 at X5(Fig. 3), which were observed in X6 and X5. Therefore, the three sand layers identified up to X11 are S1, S5, and S7 from top to bottom. The depositional ages estimated from the relationship between the thickness of the peat layer and the stratigraphic position also supports that the three layers found inland are S1, S5, and S7 (Table S3). The sand layers below Ta-c2 were difficult to compare because of limited dating, but layers S8–10 were likely comparable because of the presence of three or more sand layers on the seaward and landward sides (Fig. 2).

Sand layers S1–7 exhibited sheet distributions as far as 450–600 m inland (up to 7–11 m asl) on Line X (Figs. 5 and 8). The thicknesses of layers S1–7 exhibited trends of gradual thinning inland; eventually, the sand layers became sandy peat or unrecognizable. We focused on layers S1 and S2 to clarify their distributions over a wide area of the Erimo coast (Figs. 1 and 2). For Line Y and Z, two gray sand layers (layers S1 and S2) were identified in the peat layers above B-Tm (Fig. 2). These sand layers show a thinning trend toward the inland. S1 of Line Z has a varied thickness trend due to artificial disturbance near the surface. Their distributions could be observed along the coast for several kilometers and also inland for over 1 km along Line Z, where the topography was relatively gentle. Layer S1 was distributed further inland than S2 along all of the survey lines (Fig. 1). Layers S1 and S2 indicated that the grain sizes become gradually fined inland from medium to fine sand on Line X (Fig. 5). The grain size composition of Line Z tend to be finer inland, as in Line X, but slightly coarser, reflecting the coarser-grained river sand (Fig. 5).

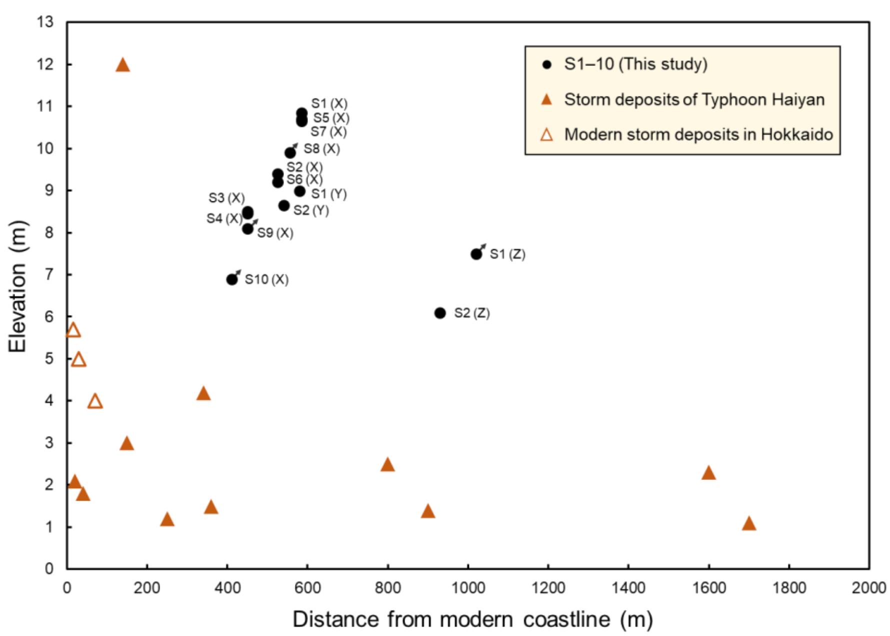

Figure 8. Distribution heights and distances from the present coastline for layers S1–10 on each survey line. The black plots with arrows indicate the sand layers that are potentially distributed farther inland due to

unconfirmed distribution limits. The letters in parentheses indicate the names of the survey lines. The filled and white triangles indicate the maximum distributions of the storm deposits of Typhoon Haiyan on the central Philippine coast and the modern storm deposits reported in Hokkaido, respectively (Brill et al., 2016; Soria et al., 2017, 2018; Nishimura & Miyaji, 1996; Ganzei et al., 2010; Shigeno & Nanayama, 2016; Chiba & Nishimura, 2018; Switzer et al., 2020). The data from Typhoon Haiyan are used for comparison as the largest storm, not as the one that actually affected Hokkaido.

4.3 Formation of anomalous sand layers

Layers S1–10 were observed in the peat with sharp boundaries with rip-up clasts (Fig. S1). The sand layers show single normal grading structures and landward grain size fining (Fig. 5). The grain size compositions of layers S1–10 were similar to those of the beach and dune sands (i.g., fine-grained offshore sands and coarse-grained river sands). The narrow grain size range of the fining trend along the survey lines can be interpreted as being due to the fact that the major sand source was well-sorted beach sand. However, because the sand layers tend to have poorer sorting than the beach sands, it is assumed that the sand layers were transported by using sand from near the estuary and offshore. The mineral assemblages also support the fact that beach sand was the major source of layers S1–10 (Fig. 6). Glauconite grains and sessile organisms, which are characteristic of offshore sediments (Noda & TuZino, 2010), were not detected in layers S1–10, which suggest that the contributions from offshore sediments are small. The sand layers were supplied from the beach sand and were transported from the sea toward the inland area, as demonstrated by the thinning and fining trends. This observation is supported by the inclusion of brackish and marine diatom valves in the sand layers, which are not present in the peat layer (Fig. 7). In addition, it is unlikely that layers S1–10 were transported by river floods because the sediments of the nearby rivers consist of gravel (Fig. 5). The Red soil is distinguished from layers S1–10 by poorly sorted sands owing to the presence of coarse-grained, low specific density amorphous components such as pumice and fine-grained detritus (Fig. 6). The repetition of sharp contrasts between peat and sand layers with rip-up clasts could have been formed only by abrupt events such as extreme waves.

Tsunamis and storm surges are known to form sand layers beyond the back barrier (e.g., Morton et al., 2007; Takashimizu et al., 2012; Brill et al., 2016). In general, although extreme waves from storms show high inundation heights, the distributions of sand layers are often limited around beach areas (Morton et al., 2007; Watanabe et al., 2018). Storm surges also consist of gradual rises in the water level, which inundate beaches from the lowest points. Thus, storm deposit distributions are often scattered and lobe-shaped (Nishimura & Miyaji, 1996; Brill et al., 2016; Chiba & Nishimura, 2018). Storm deposits have also been reported in Hokkaido, and their distributions were reported up to 4–6 m asl and a few tens of meters from the shoreline (Nishimura & Miyaji, 1996; Ganzei et al., 2010; Shigeno & Nanayama, 2016; Chiba & Nishimura, 2018; Switzer et al., 2020). Additionally, tsunamis result in erosion and inland transportation of large sediment volumes in short time intervals (Morton et al., 2007; Szczuciński et al., 2012; Goto et al., 2014). As a result of erosion, the contacts between the transported sand layers and the background sediments are very sharp and often include rip-up clasts (Szczuciński et al., 2012; Takashimizu et al., 2012). Inundation flows are slowed by flooding on land; grains with higher specific gravity settle and are eventually recorded in the sediment as grading structures (Jaffe et al., 2012; Yoshii et al., 2017). The amounts of transported sediments are limited owing to decreasing tsunami flow velocities and inundation depths; thus, sheet-like distributions and gradual thinning are observed (Szczuciński et al., 2012; Takashimizu et al., 2012; Goto et al., 2014).

By comparing the features of the modern tsunami and storm deposits described above, it was shown that the sand layers in this area are tsunami deposits. Layers S1–10 exhibited normal grading and sharp basal contacts with rip-up clasts; these sedimentary structures indicate erosional flow and decreased velocities of single flows. Their distributions extended to several hundred meters inland from the beach and they are spread over wide areas along the shoreline. In addition, the elevations of the sand layer distributions are at least 7–11 m asl (Fig. 8), which is significantly higher than those of modern storm deposits (Nishimura & Miyaji, 1996; Ganzei et al., 2010; Brill et al., 2016; Shigeno & Nanayama, 2016; Soria et al., 2017, 2018; Chiba & Nishimura, 2018; Switzer et al., 2020). The elevations of the deposits are > 5 m asl even when considering the relative sea levels of the past 4000 years based on hydro-isostasy and crustal uplift (up to + 2.1 m at a mean higher high water level: Koike & Machida, 2001; Okuno et al., 2014). For the past 4000 years, the Erimo coast has been limited to the area located ~100 m from the present coastline with elevations under 2 m asl. Therefore, the distributions of layers S1–10 along Line X are estimated to be present for more than 300–500 m from the past coastline. Considering that the distributions of layers S1–10 cannot be explained by anomalous storms and that some sedimentary structures are common in tsunami deposits, these are interpreted as anomalous sand layers that were deposited by high tsunami waves.

5 Numerical simulations

We used numerical simulations to reconstruct tsunami inundation consistent with observed distributions of tsunami deposits along the eastern Hokkaido coast. Tsunamis generated by Mw~8 earthquakes in the Kuril Trench are known to have recurrence periods of several decades (e.g., the 1952 and 2003 Tokachi-oki earthquakes). Given that no sandy deposits were transported into the back barrier by these tsunamis (Nishimura et al., 2004), it is unlikely that the tsunamis generated by Mw~8 earthquakes transported the S1–10 tsunami deposits. A source rupture model based on geological data has been proposed for 17th-century earthquakes (Nanayama et al., 2003; Satake et al., 2008; Ioki & Tanioka, 2016). The T10N5S25 model (Mw 8.8, where T10 denotes 10 m slip on the Tokachi-oki segment, N5 denotes 5 m slip on the Nemuro segment, and S25 denotes 25 m slip on the shallow part segment; Fig. 1) produces an inundation area that covers the distribution of the tsunami deposits extending from the Tokachi to Nemuro regions (Ioki & Tanioka, 2016). In addition to the distribution of tsunami deposits, these source rupture models are required to meet the constraint that tsunami wave heights should not exceed 3 m in the Sanriku region because there is no description of an earthquake like this in the historical documents (Satake et al., 2008). However, this requirement has not yet been appropriately satisfied.

We tested whether the T10N5S25 model can be applied to 17th-century tsunami deposits in the Erimo area, which are further to the west. The resulting inundation area did not cover the entire distribution of layer S1 (Fig. 9). To avoid affecting the tsunami simulation results in the Tokachi to Nemuro regions, we attempted to adjust the fault model to expand the tsunami inundation area in the Erimo area. If, in the Tokachi-oki segment, the rupture model parameter is wider or the slip amount is increased, the maximum wave height along the Sanriku coast will be higher. Therefore, we attempted to reproduce the inundation area in the Erimo area by narrowing the fault width, as it is known that the wavelengths affect inundation extents depending on the topography (Satake et al., 2013). The fault widths were set at 10 km intervals that ranged from

40 to 90 km (T10w40–T10w90) along the Tokachi-oki segment; N5 and S25 are constant for all conditions. The magnitudes of these rupture models were Mw 8.7–8.8.

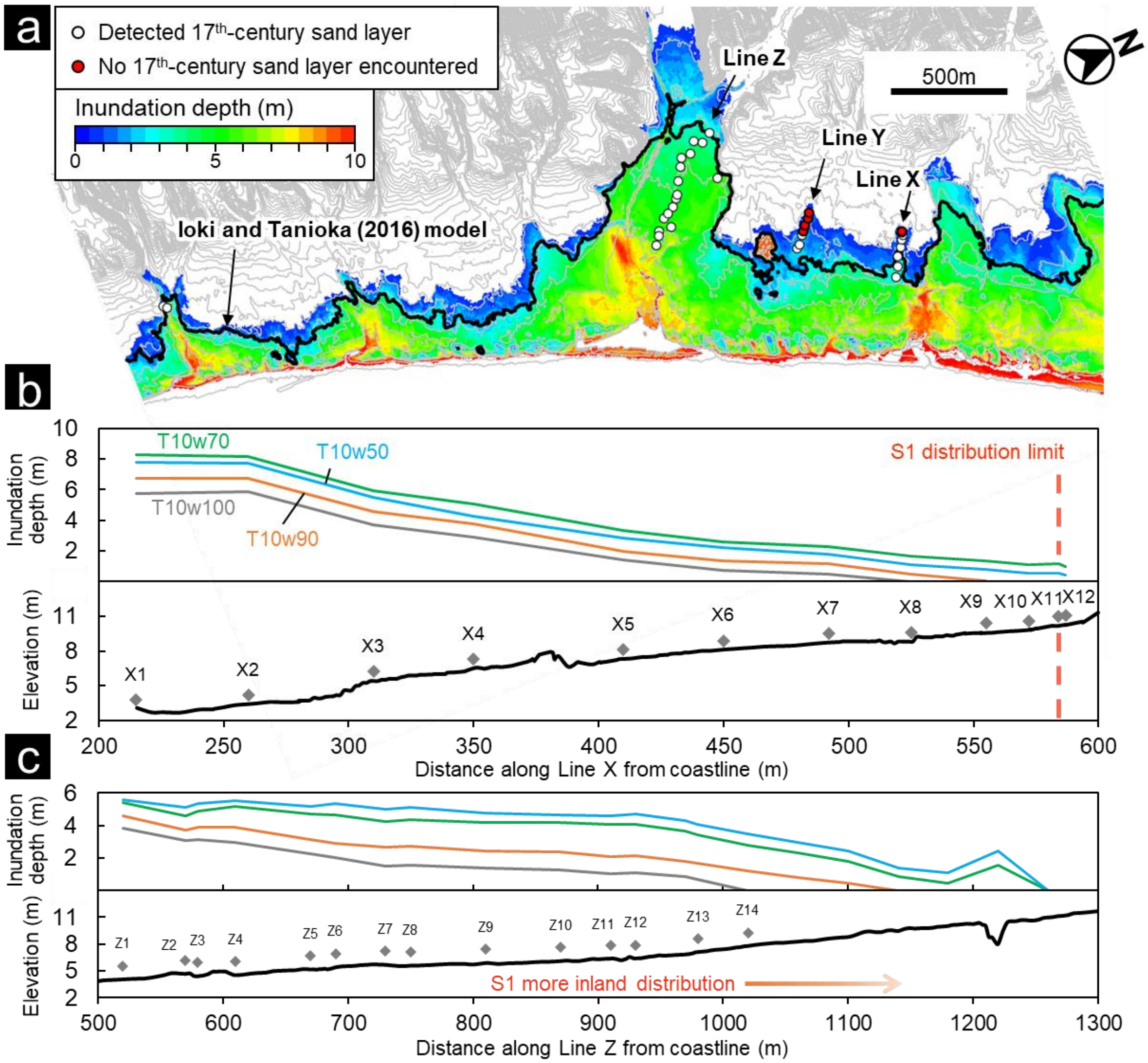

Figure 9. Simulation results of tsunami run-ups on the Erimo coast. a: Tsunami inundation area using the Ioki & Tanioka (2016) model (black line) and T10w70 model (colors). b: Tsunami inundation depth profiles for each fault width value and the topographic profile on Line X. c: Tsunami inundation depth profiles and the topographic profile on Line Z. T10w100 is a conventional model (Ioki & Tanioka, 2016)

The T10w50–T10w70 models generated inundation areas that covered the entire distribution of layer S1 (Fig. 9). These models also changed the energy directivity to the Sanriku region, such that the maximum wave heights on the Sanriku coastline decreased as the fault widths narrowed (Fig. S5). The maximum wave heights along the coastline from the Tokachi to Nemuro regions also exhibited slight decreases when narrow fault width conditions were used.

The T10w70 model is more reasonable because it reproduces an inundation area that covers a sufficient amount of tsunami deposits and minimizes the wave height changes from the Tokachi to Nemuro regions.

In these numerical simulations, we used a simple modification method that consisted of changing the fault width of the Tokachi-oki segments, and it can be explained that the inundation area extended wider for several reasons. The crustal deformation of this model exhibits a subsidence level of ~15 cm around Erimo (Fig. S6), while the model proposed by Ioki & Tanioka (2016) exhibited a subsidence level of ~40 cm, which does not explain the differences in the inundation extents. The locally high wave heights in the Erimo area likely reflected the shortening of the wave periods that was caused by the narrowing of the fault width. When the fault width of T10 is 100 km, there is a certain interval between the first and second waves, but the T10w70 model shows that the first wave propagates slightly more slowly and excites the second wave (Fig. 10). In addition, in the T10w70 model, the third wave appears earlier and merges with the wave that is trapped by the shallow bathymetry on the Cape Erimo extension and expands the inundation area subsequent to the second wave. The landward side of X5 was inundated only by the first wave (Fig. 10). This is consistent with the fact that the observed sedimentary structure of the sand layers consisted of single normal grading (Fig. 5). The T10w70 model is nearly equal to Mw 8.8, which is the same scale as the conventional model. This means that the model based on the tsunami deposits from the Tokachi to Nemuro region can reproduce the tsunami deposit distributions found on the eastern Erimo coast without major changes. Since it is known that actual rupture zones are not rectangular but are heterogeneous (e.g., Liu et al., 2013), it should be noted that the model does not necessarily recover the detailed parameters of the source fault. By taking this information into account, a simulation could reproduce the tsunami deposit distributions in each region with greater accuracy. On the other hand, it should be noted that the distributions of the sand layers contain uncertainties because tsunami deposits are known poor preservation by postdepositional processes (Richmond et al., 2012; Szczuciński, 2020), and tsunami inundations limited sand can only be transported (Abe et al., 2012). To reduce such uncertainties, it is necessary to evaluate the tsunami inundation areas by using chemical and biomarker methods that are independent of the sand layers (e.g., Szczuciński et al., 2016; Chagué-Goff et al., 2017).

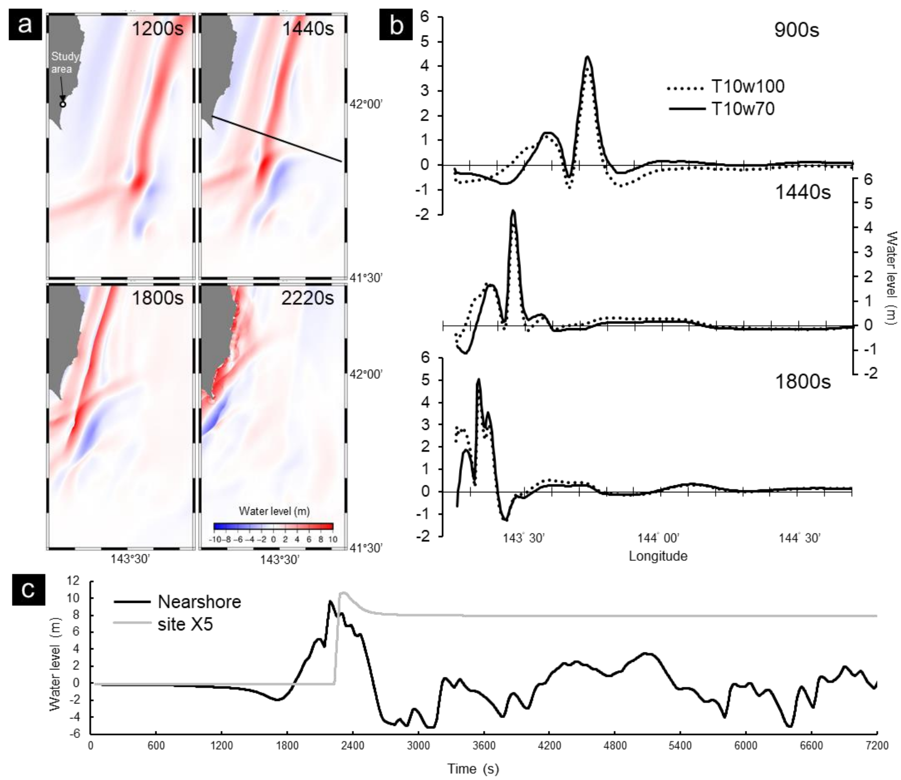

Figure 10. Tsunami waveforms in the time series from the numerical simulations of the 17th-century tsunami. a: Temporal changes in water level for the T10w70 model. Snapshots taken at 1200, 1440, 1800, and 2220 seconds after the earthquake. The black line indicates the survey line shown in Figure 10b. b: The wave profiles on the black line shown in Fig. 10a at 900, 1440, and 1800 seconds for the T10w100 and T10w70 models. c: Time series of the tsunami waveforms of the T10w70 model at site X5 and nearshore of Line X. The DEM elevation at site X5 is 7.9 m asl.

6 Correlation of tsunami deposits

Regional comparison of tsunami events was made by assessing the consistency of tsunami ages in the surrounding areas. Tsunami ages have been reported in the Tokachi (Urahoro) and Hidaka (Utoma) regions (Ishizawa et al., 2017; Nakanishi et al., 2020a). The agreements of the probability density functions of events that were obtained by the sequencing model for each region were calculated using the overlapping coefficient (OVL: Inman &

Bradley, 1989; Hutchinson & Clague, 2017: Table 2). Hutchinson & Clague (2017) adopted critical threshold values for probable coeval events when the OVLs were > 0.25.

We compared the depositional ages of the sand layers with those reported for Urahoro and Utoma, which were measured using the same ^{14}C dating method (Fig. 11). In the Erimo and Urahoro areas facing the Tokachi-oki segment, the depositional ages were comparable in all of the observed sand layers, and the OVLs ranged from 0.39 to 0.78 (Table 2). In particular, S2 and L2 (layer 2 in Urahoro: Ishizawa et al., 2017) showed a narrow range from ~800 to 700 BP, with an error of 20 years. The results mean that Urahoro and Erimo recorded the same numbers of large tsunamis that occurred at the same times during the past 3000 years. In the Utoma area, which is located on the southern Hidaka coast, the depositional ages are comparable in the four sand layers, except for U3 (sand layer interpreted as a tsunami deposit in Utoma: Nakanishi et al., 2020a), and the OVLs range from 0.26 to 0.81 (Table 2). The geological record in Utoma is currently limited to the period before 2,000 BP, but tsunamis with recurrence intervals of ~430 years are most likely to have been generated by the common Mw>8 earthquakes in the Tokachi region. However, it is necessary to consider the possibility that tsunamis from different sources, such as the U3 event in Utoma, are also included in the data.

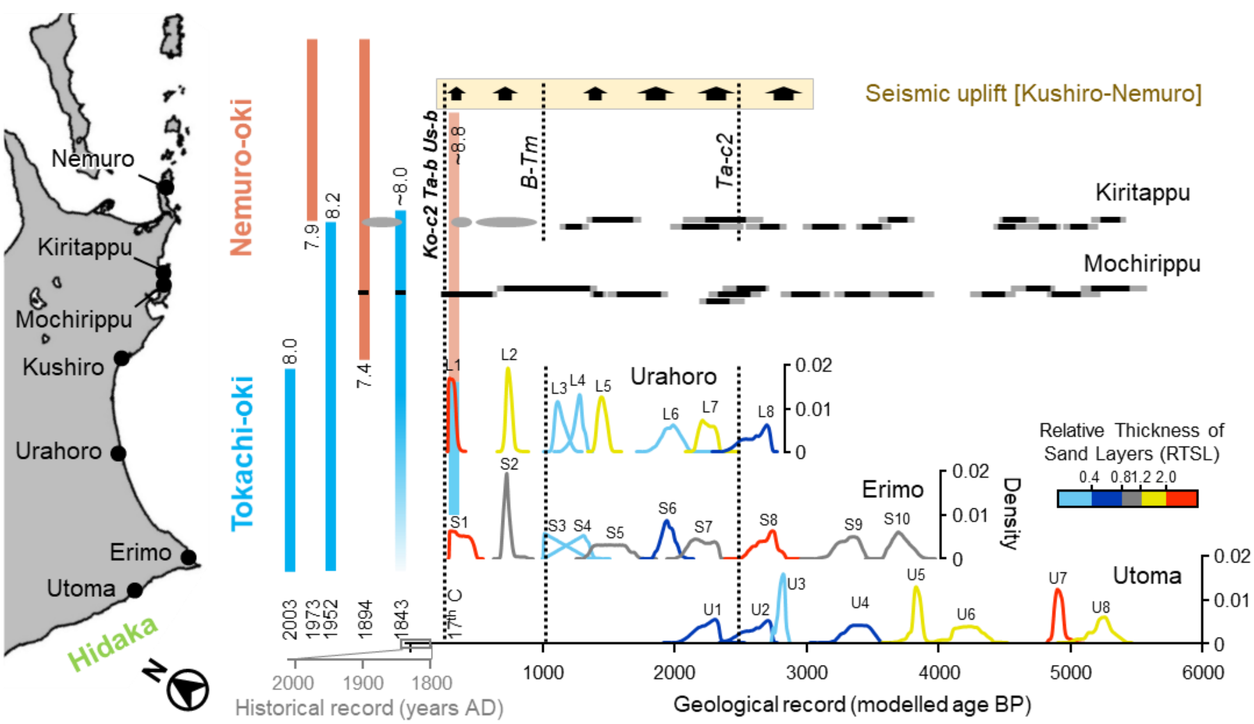

Figure 11. Depositional ages of sand layers in the Hidaka and Tokachi regions (Ishizawa et al., 2017; Nakanishi et al., 2020a). The depositional ages are presented as probability density functions. The color scale of the histograms indicates the relative thicknesses of the sand layers, which were normalized using the median values and exclude any outliers. Outliers were defined as exceeding the interquartile range by 1.5 times based on the upper quartile. Gray and black bars indicate the estimated ages (2σ and 1σ, respectively) of the

tsunamis reported in the Mochirippu and Kiritappu areas (Sawai et al., 2009). Black arrows indicate the age ranges of the seismic uplifts in the Kushiro to Nemuro regions (Kelsey et al., 2006). Blue and red color bars indicate the fault lengths of earthquakes that occurred off the Tokachi and Nemuro coasts, respectively (Satake, 2015). The numbers beside each color bar indicate the moment magnitudes of the earthquakes.

Table 2. The depositional ages of the compared events obtained by the sequence model and the overlapping coefficients (OVL).

Urahoro*1	2 σ range modeled age (BP)		Erimo	2 σ range modeled age (BP)		OVL
L1	350	283	S1	474	287	0.42
L2	786	704	S2	796	680	0.72
L3	1214	1070	S3	1279	1003	0.53
L4	1340	1184	S4	1372	1068	0.63
L5	1511	1400	S5	1704	1348	0.39
L6	2097	1845	S6	2043	1851	0.78
L7	2336	2166	S7	2340	2069	0.65
L8	2735	2442	S8	2825	2546	0.63
Ave.						0.59

Erimo	2 σ range modeled age (BP)		Utoma*2	2 σ range modeled age (BP)		OVL
S7	2340	2069	U1	2356	2071	0.81
S8	2825	2546	U2	2743	2438	0.67
S9	3449	3170	U4	3542	3234	0.66
S10	3846	3590	U5	3905	3735	0.26
Ave.						0.60

Urahoro	2 σ range modeled age (BP)		Utoma	2 σ range modeled age (BP)		OVL
L7	2336	2166	U1	2356	2071	0.76
L8	2735	2442	U2	2743	2438	0.95
Ave.						0.86

*1: Ishizawa et al. (2017)
*2: Nakanishi et al. (2020a)

The relative thicknesses of the sand layers (RTSL), which are normalized by the median values of all sand layers within the core, suggest that Tokachi and Hidaka regions experienced tsunamis of similar magnitude (Fig. 11). In Erimo and Urahoro, it is very interesting to match the patterns of the high and low values, except for layer S8. This good agreement between the two regions, despite the 100 km distance between them, may support the assumption that both regions experienced tsunamis of similar magnitudes. This is because modern tsunami deposit studies infer that the thicknesses of tsunami deposits are most sensitive to the inundation depths (Goto et al., 2014; Naruse & Abe, 2017). However, it should be noted that the microtopography, accommodation space, sediment source, and postdepositional changes all significantly influence the thicknesses of tsunami deposits (Szczuciński, 2020). Actually, the RTSL in Utoma is thick in the sand layers that were deposited at approximately 5000 BP, which was due to the influence of the sea level highstand in the mid-Holocene (Nakanishi et al., 2020a).

Several tsunami deposits can be correlated along more than 150 km of the coast, which suggests that they were generated by tsunamis that resulted from Mw>8 earthquakes, with fault lengths of several hundred kilometers. Therefore, few of the layer S1–10 events are expected to be correlated with the geological evidence identified from the Kushiro to Nemuro regions for paleo-earthquakes (Nanayama et al., 2003; Sawai et al., 2004, 2009; Kelsey et al., 2006). The tsunami ages and seismic crustal movements in Kiritappu and Mochirippu have been estimated based on ^{14}C dating (Sawai et al., 2009). However, direct correlations are difficult because of the differences in the sample materials, dating methods, and dating depth points. The estimated ages of the seismic uplifts in the Nemuro to Kushiro regions (Kelsey et al., 2006) appear to correlate with the depositional ages of the relatively thick sand layers found in the Hidaka and Tokachi regions (e.g., layers S1, S5, and S7). The distributions of these layers are most extensive inland (Fig. 2). Thus, these tsunamis might have been generated by higher-magnitude earthquakes or by wider rupture zones when compared with other events from the Tokachi to Hidaka regions.

The observed earthquakes along the Japan Trench caused 3–4 m tsunamis in the Erimo area, and may have caused larger tsunamis in prehistoric periods (Nakanishi et al., 2020a). The 1611 Keicho tsunami is considered to be the largest tsunami among those of historical earthquakes recorded in documents of the Sanriku region. Although it is not known how high this tsunami reached along the Hokkaido coast (Sawai, 2020), Tetsuka et al. (2020) simulated a tsunamis generated by Mw8.8 earthquakes off the Sanriku coast and showed that a large tsunami would not reach the Hokkaido coast. However, some paleo-tsunami deposits in the Sanriku region show similar ages to those in the Erimo area (e.g., Ishizawa et al., 2022). Therefore, some for events there is a need to consider a wave source in (or across) the Japan Trench.

The Nemuro and Tokachi-Hidaka regions likely experienced different paletosunami histories based on the numbers of sand layers recorded at well-studied sites. Thus, both regions likely experienced at least some different paleotsunamis. Cataloging megathrust earthquakes shows that the rupture segmentation and cyclicity can be complex (Philibosian & Meltzner, 2020), and the Kuril Trench is no exception, which suggests that the regions that are located across the currently known segments have different rupture histories. Information on the earthquake segmentation in this trench and their recurrence intervals will better explain the megathrust earthquake mechanisms and hazard assessments.

7 Conclusions

We identified ten anomalous sand layers in the coastal wetland in Erimo, Hokkaido, Japan. These sand layers share similarities with beach sands and can be distinguished from aeolian and river sands. Moreover, they share common features with modern tsunami deposits, such as normal grading structures and sharp basal contacts with rip-up clasts. The sand layers are distributed at distances of several hundred meters from the shoreline (up to 7–11 m asl), which cannot be explained by extreme storms or tsunamis caused by Mw~8 earthquakes. Numerical simulations were performed for a 17th-century tsunami to examine whether the distributions of the 17th-century sand layers could be reproduced by the Mw 8.8 earthquake model. The results showed that tsunami inundation by conventional models was insufficient to cover the distribution of tsunami deposits. We modified the fault width slightly without changing the tsunami wave heights in the eastern area, and found that it was possible to reproduce the distribution of tsunami deposits in the Erimo area. The correlations of tsunami events in the past 4000 years imply widespread deposition of sand by large tsunamis that impacted the Tokachi and Hidaka regions and indicate recurrence intervals of 110–620 years. The chronological correlations between most of the tsunamis at these sites indicate that the paleotsunamis reported in eastern Hokkaido reached the Hidaka region. On the other hand, a detailed study of the tsunami ages also revealed the differences between the regions that face the Tokachi-oki and Nemuro-oki segments, suggesting the diversity of the Kuril earthquakes every few hundred years. By extending the correlations of the paleotsunamis from Hidaka to Tokachi to the past 4000 years, the spatial extents and recurrence intervals of large tsunamis in the regions that face the Tokachi-oki segment have been significantly updated. The common history of the tsunamis in the area facing the Tokachi-oki segment that are revealed by this study will provide a framework for more comprehensive correlations of the Mw>8 earthquakes in the entire Kuril Trench.

Acknowledgments

The authors would like to thank S. Ishikawa from the Erimo town office for allowing us to conduct the field surveys. We appreciate the valuable comments by Y. Sawai and K. Ioki (AIST). This research was supported by Grants-in-Aid from the JSPS to R. Nakanishi (20J21239) and to Y. Yokoyama (20H00193). This study was performed under the cooperative research program of Center for Advanced Marine Core Research (CMCR), Kochi University 〈Accept No. 20A010 and 21B042〉.

Data Availability Statement

The new ^{14}C datasets for this research are provided in Table 1 in this paper. We used the tsunami calculation code JAGURS (Baba et al., 2015, 2017) at https://doi.org/10.5281/zenodo.3737816. Generic mapping tools were used to draw the figures (Wessel et al., 2013).

References

Abe, T., Goto, & K., Sugawara, D. (2012). Relationship between the maximum extent of tsunami sand and the inundation limit of the 2011 Tohoku-oki tsunami on the Sendai Plain, Japan. Sedimentary Geology, 282, 142–150. https://doi.org/10.1016/j.sedgeo.2012.05.004

Baba, T., Takahashi, N., Kaneda, Y., Ando, K., Matsuoka, D., & Kato, T. (2015). Parallel Implementation of Dispersive Tsunami Wave Modeling with a Nesting Algorithm for the 2011 Tohoku Tsunami. Pure and Applied Geophysics, 172(12), 3455–3472. https://doi.org/10.1007/s00024-015-1049-2

Baba, T., Allgeyer, S., Hossen, J., Cummins, P. R., Tsushima, H., Imai, K., et al. (2017). Accurate numerical simulation of the far-field tsunami caused by the 2011 Tohoku earthquake, including the effects of Boussinesq dispersion, seawater density stratification, elastic loading, and gravitational potential change. Ocean Modelling, 111, 46–54. https://doi.org/10.1016/j.ocemod.2017.01.002

Brill, D., May, S. M., Engel, M., Reyes, M., Pint, A., Opitz, S., et al. (2016). Typhoon Haiyan's sedimentary record in coastal environments of the Philippines and its palaeotempestological implications. Natural Hazards and Earth System Sciences, 16(12), 2799–2822. https://doi.org/10.5194/nhess-16-2799-2016

Bronk Ramsey, C. (2008). Deposition models for chronological records. Quaternary Science Reviews, 27(1), 42–60. https://doi.org/10.1016/j.quascirev.2007.01.019

Bronk Ramsey, C. (2009a). Bayesian Analysis of Radiocarbon Dates. Radiocarbon, 51(1), 337–360. https://doi.org/10.1017/S0033822200033865

Bronk Ramsey, C. (2009b). Dealing with Outliers and Offsets in Radiocarbon Dating. Radiocarbon, 51(3), 1023–1045. https://doi.org/10.1017/S0033822200034093

Chagué-Goff, C., Szczuciński, W., & Shinozaki, T. (2017). Applications of geochemistry in tsunami research: A review. Earth-Science Reviews, 165, 203–244. https://doi.org/10.1016/j.earscirev.2016.12.003

Chiba, T., & Sawai, Y. (2014). Reexamination and updating of diatom species for paleoenvironmental reconstructions. Diatom, 30, 17–30 (in Japanese, with English abstract).

Chiba, T., & Nishimura, Y. (2018). Depositional processes of the storm surge deposits due to Typhoon 1523 in Horokayanto, Hokkaido, Japan. The Quaternary Research (Daiyonki kenkyu), 57, 53–63 (in Japanese, with English abstract).

Folk, R. L., & Ward, W. C. (1957). Brazos river bar: A study in the significance of grain size parameters. Journal of Sedimentary Petrology, 27(1), 3–26. https://doi.org/10.1306/74D70646-2B21-11D7-8648000102C1865D

Ganzei, L. A., Razzhigaeva, N. G., Harlamov, A. A., & Ivel'skaya, T. N. (2010). Extreme storms in 2006–2007 on Shikotan Island and their impact on the coastal relief and deposits. Oceanology, 50(3), 425–434. https://doi.org/10.1134/S0001437010030112

Goldfinger, C., Ikeda, Y., Yeats, R. S., & Ren, J. (2013). Superquakes and Supercycles. Seismological Research Letters, 84(1), 24–32. https://doi.org/10.1785/0220110135

Goto, K., Hashimoto, K., Sugawara, D., Yanagisawa, H., & Abe, T. (2014). Spatial thickness variability of the 2011 Tohoku-oki tsunami deposits along the coastline of Sendai Bay. Marine Geology, 358, 38–48. https://doi.org/10.1016/j.margeo.2013.12.015

Hashimoto, C., Noda, A., Sagiya, T., & Matsu'ura, M. (2009). Interplate seismogenic zones along the Kuril–Japan trench inferred from GPS data inversion. Nature Geoscience, 2(2), 141–144. https://doi.org/10.1038/ngeo421

Hutchinson, I., & Clague, J. (2017). Were they all giants? Perspectives on late Holocene plate-boundary earthquakes at the northern end of the Cascadia subduction zone. Quaternary Science Reviews, 169, 29–49. https://doi.org/10.1016/j.quascirev.2017.05.015

Inman, H. F., & E. L. Bradly Jr. (1989). The overlapping coefficient as a measure of agreement between probability distributions and point estimation of the overlap of two normal densities. Communications in Statistics - Theory and Methods, 18(10), 3851–3874. https://doi.org/10.1080/03610928908830127

Ioki, K., & Tanioka, Y. (2016). Re-estimated fault model of the 17th century great earthquake off Hokkaido using tsunami deposit data. Earth and Planetary Science Letters, 433, 133–138. https://doi.org/10.1016/j.epsl.2015.10.009

Ishizawa, T., Goto, K., Yokoyama, Y., Miyairi, Y., Sawada, C., Nishimura, Y., & Sugawara, D. (2017). Sequential radiocarbon measurement of bulk peat for high-precision dating of tsunami deposits. Quaternary Geochronology, 41, 202–210. https://doi.org/10.1016/j.quageo.2017.05.003

Ishizawa, T., Goto, K., Yokoyama, Y., & Goff, J. (2020). Dating tsunami deposits: Present knowledge and challenges. Earth-Science Reviews, 200, 102971. https://doi.org/10.1016/j.earscirev.2019.10297

Ishizawa, T., Goto, K., Nishimura, Y., Miyairi, Y., Sawada, C., & Yokoyama, Y. (2022). Paleotsunami history along the northern Japan trench based on sequential dating of the continuous geological record potentially inundated only by large tsunamis. Quaternary Science Reviews, 279, 107381. https://doi.org/10.1016/j.quascirev.2022.107381

Jaffe, B. E., Goto, K., Sugawara, D., Richmond, B. M., Fujino, S., & Nishimura, Y. (2012). Flow speed estimated by inverse modeling of sandy tsunami deposits: results from the 11 March 2011 tsunami on the coastal plain near the Sendai Airport, Honshu, Japan. Sedimentary Geology, 282, 90–109. https://doi.org/10.1016/j.sedgeo.2012.09.002

Jagodziński, R., Sternal, B., Szczuciński, W., Chagué-Goff, C., & Sugawara, D. (2012). Heavy minerals in the 2011 Tohoku-oki tsunami deposits—insights into sediment sources and hydrodynamics. Sedimentary Geology, 282, 57–64. https://doi.org/10.1016/j.sedgeo.2012.07.015

Kelsey, H., Satake, K., Sawai, Y., Sherrod, B., Shimokawa, K., & Shishikura, M. (2006). Recurrence of postseismic coastal uplift, Kuril subduction zone, Japan. Geophysical Research Letters, 33(13), L13315. https://doi.org/10.1029/2006GL026052

Koike, K. & Machida, H. (2001). Atlas of Quaternary Marine Terraces in the Japanese Islands: Tokyo, University of Tokyo Press (in Japanese).

Lienkaemper, J. J., & Ramsey, C. B. (2009). OxCal: Versatile Tool for Developing Paleoearthquake Chronologies –A Primer. Seismological Research Letters, 80(3), 431–434. https://doi.org/10.1785/gssrl.80.3.431

Liu, X., Zhao, D., & Li, S. (2013). Seismic heterogeneity and anisotropy of the southern Kuril arc: insight into megathrust earthquakes. Geophysical Journal International, 194(2), 1069–1090. https://doi.org/10.1093/gji/ggt150

Morton, R. A., Gelfenbaum, G., & Jaffe, B. E. (2007). Physical criteria for distinguishing sandy tsunami and storm deposits using modern examples. Sedimentary Geology, 200(3–4), 184–207. https://doi.org/10.1016/j.sedgeo.2007.01.003

Nakamura, Y., Nishimura, Y., & Putra, P. S. (2012). Local variation of inundation, sedimentary characteristics, and mineral assemblages of the 2011 Tohoku-oki tsunami on the Misawa coast, Aomori, Japan. Sedimentary Geology, 282, 216–227. https://doi.org/10.1016/j.sedgeo.2012.06.003

Nakanishi, R., Okamura, S., Yokoyama, Y., Miyairi, Y., Sagayama, T., & Ashi, J. (2020a). Holocene tsunami, storm, and relative sea level records obtained from the southern Hidaka coast, Hokkaido, Japan. Quaternary Science Reviews, 250, 106678. https://doi.org/10.1016/j.quascirev.2020.106678

Nakanishi, R., Ashi, J., & Okamura, S. (2020b). A dataset for distribution and characteristics of Holocene pyroclastic fall deposits along the Pacific coasts in western Hokkaido, Japan. Data in Brief, 33, 106565. https://doi.org/10.1016/j.dib.2020.106565

Nanayama, F., Satake, K., Furukawa, R., Shimokawa, K., Atwater, B. F., Shigeno, K., & Yamaki, S. (2003). Unusually large earthquakes inferred from tsunami deposits along the Kuril trench. Nature, 424(6949), 660–663. https://doi.org/10.1038/nature01864

Nanayama, F., Furukawa, R., Shigeno, K., Makino, A., Soeda, Y., & Igarashi, Y. (2007). Nine unusually large tsunami deposits from the past 4000 years at Kiritappu marsh along the southern Kuril Trench. Sedimentary Geology, 200(3–4), 275–294. https://doi.org/10.1016/j.sedgeo.2007.01.008

Naruse, H., & Abe, T. (2017). Inverse Tsunami Flow Modeling Including Nonequilibrium Sediment Transport, With Application to Deposits From the 2011 Tohoku-Oki Tsunami. Journal of Geophysical Research: Earth Surface, 122(11), 2159–2182. https://doi.org/10.1002/2017JF004226

Nelson, A. R., Kelsey, H. M., & Witter, R. C. (2006). Great earthquakes of variable magnitude at the Cascadia subduction zone. Quaternary Research, 65(3), 354–365. https://doi.org/10.1016/j.yqres.2006.02.009

Nishimura, Y., & Miyaji, N. (1996). Investigations of storm deposits caused by a typhoon of September 19th, 1994. Bulletin of the Natural Disaster Science Data Center, Hokkaido, 10, 15–26 (in Japanese, with English abstract).

Nishimura Y., Tanioka Y., & Hirakawa K. (2004). Beachside Trace for the 2003 Tokachi-oki Tsunami Run-up. Zisin (Journal of the Seismological Society of Japan. 2nd ser.), 57(2), 135–138. https://doi.org/10.4294/zisin1948.57.2_135

Noda, A., & TuZino, T. (2010). Shelf–slope sedimentation during the late Quaternary on the southwestern Kuril forearc margin, northern Japan. Sedimentary Geology, 232(1–2), 35–51. https://doi.org/10.1016/j.sedgeo.2010.09.008

Noda, A., & Katayama, H. (2011) Sedimentological Map Offshore of Cape Erimo. Marine Geology Map Series, no. 72, Geological Survey of Japan, AIST.

Okada, Y. (1985). Surface deformation due to shear and tensile faults in a half-space, Bulletin of the Seismological Society of America, 75, 1135–1154.

Okuno, J., Nakada, M., Ishii, M., & Miura, H. (2014). Vertical tectonic crustal movements along the Japanese coastlines inferred from late Quaternary and recent relative sea-level changes. Quaternary Science Reviews, 91, 42–61. https://doi.org/10.1016/j.quascirev.2014.03.010

Philibosian, B., & Meltzner, A. J. (2020). Segmentation and supercycles: A catalog of earthquake rupture patterns from the Sumatran Sunda Megathrust and other well-studied faults worldwide. Quaternary Science Reviews, 241, 106390. https://doi.org/10.1016/j.quascirev.2020.106390

Reimer, P. J., Austin, W. E. N., Bard, E., Bayliss, A., Blackwell, P. G., Ramsey, C. B., et al. (2020). The IntCal20 Northern Hemisphere Radiocarbon Age Calibration Curve (0–55 cal kBP). Radiocarbon, 62(4), 725–757. https://doi.org/10.1017/RDC.2020.41

Richmond, B., Szczuciński, W., Chagué-Goff, C., Goto, K., Sugawara, D., Witter, R., et al. (2012). Erosion, deposition and landscape change on the Sendai coastal plain, Japan, resulting from the March 11, 2011 Tohoku-oki tsunami. Sedimentary Geology, 282, 27–39. https://doi.org/10.1016/j.sedgeo.2012.08.005

Sakuraba, H. (2019). Cape Erimo National Forest Management Project (Erimo Town, Hokkaido), Suirikagaku, 62, 119–124 (in Japanese). https://doi.org/10.20820/suirikagaku.62.6_119

Salditch, L., Stein, S., Neely, J., Spencer, B. D., Brooks, E. M., Agnon, A., & Liu, M. (2020). Earthquake supercycles and Long-Term Fault Memory. Tectonophysics, 774, 228–289. https://doi.org/10.1016/j.tecto.2019.228289

Satake, K. (2015). Geological and historical evidence of irregular recurrent earthquakes in Japan. Philosophical Transactions of the Royal Society A: Mathematical, Physical and Engineering Sciences, 373(2053), 20140375. https://doi.org/10.1098/rsta.2014.0375

Satake, K., Nanayama, F., & Yamaki, S. (2008). Fault models of unusual tsunami in the 17th century along the Kuril trench. Earth, Planets and Space, 60(9), 925–935. https://doi.org/10.1186/BF03352848

Satake, K., Fujii, Y., Harada, T., Namegaya, N. (2013). Time and Space Distribution of Coseismic Slip of the 2011 Tohoku Earthquake as Inferred from Tsunami Waveform Data. Bulletin of the Seismological Society of America, 103 (2B), 1473–1492. https://doi.org/10.1785/0120120122

Sawai, Y., Satake, K., Kamataki, T., Nasu, H., Shishikura, M., Atwater, B. F., et al. (2004). Transient Uplift After a 17th-Century Earthquake Along the Kuril Subduction Zone. Science, 306(5703), 1918–1920. https://doi.org/10.1126/science.1104895

Sawai, Y., Kamataki, T., Shishikura, M., Nasu, H., Okamura, Y., Satake, K., et al. (2009). Aperiodic recurrence of geologically recorded tsunamis during the past 5500 years in eastern Hokkaido, Japan. Journal of Geophysical Research: Solid Earth, 114, B01319. https://doi.org/10.1029/2007JB005503

Sawai, Y. (2020). Subduction zone paleoseismology along the Pacific coast of northeast Japan — progress and remaining problems. Earth-Science Reviews, 208, 103261. https://doi.org/10.1016/j.earscirev.2020.103261

Sella, G. F., Dixon, T. H., & Mao, A. (2002). REVEL: A model for Recent plate velocities from space geodesy: REVEL-RECENT PLATE VELOCITIES FROM SPACE GEODESY. Journal of Geophysical Research: Solid Earth, 107(B4), ETG 11-1-ETG 11-30. https://doi.org/10.1029/2000JB000033

Shigeno, K., & Nanayama, F. (2016). Sedimentary Process of a Small Sandy Event Deposit due to a Storm Surge and Storm Waves Generated by a Typhoon: An Example from the Hirahama Coastal Lowland along the Western Example from the Hirahama Coastal Lowland along the Western Coast of the Oshima Peninsula between 09:00 September 18 and 01:00 September 19, 1959. Journal of Geography (Chigaku Zasshi), 125, 747–762 (in Japanese, with English abstract). https://doi:10.5026/jgeography.125.747

Sieh, K., Natawidjaja, D. H., Meltzner, A. J., Shen, C.-C., Cheng, H., Li, K.-S., et al. (2008). Earthquake Supercycles Inferred from Sea-Level Changes Recorded in the Corals of West Sumatra. Science, 322(5908), 1674–1678. https://doi.org/10.1126/science.1163589

Soria, J. L. A., Switzer, A. D., Pilarczyk, J. E., Siringan, F. P., Khan, N. S., & Fritz, H. M. (2017). Typhoon Haiyan overwash sediments from Leyte Gulf coastlines show local spatial variations with hybrid storm and tsunami signatures. Sedimentary Geology, 358, 121–138. https://doi.org/10.1016/j.sedgeo.2017.06.006

Soria, J. L. A., Switzer, A. D., Pilarczyk, J. E., Tang, H., Weiss, R., Siringan, F., et al. (2018). Surf beat-induced overwash during Typhoon Haiyan deposited two distinct sediment assemblages on the carbonate coast of Hernani, Samar, central Philippines. Marine Geology, 396, 215–230.

Szczuciński, W. (2020). Post-depositional changes to tsunami deposits and their preservation potential. In M. Engel, J. Pilarczyk, S. Matthias, M. D. Brill, & Ed Garrett (Eds.), Geological records of tsunamis and other extreme waves. Elsevier. https://doi.org/10.1016/B978-0-12-815686-5.00021-3

Szczuciński, W., Kokociński, M., Rzeszewski, M., Chagué-Goff, C., Cachão, M., Goto, K., & Sugawara, D. (2012). Sediment sources and sedimentation processes of 2011 Tohoku-oki tsunami deposits on the Sendai Plain, Japan — Insights from diatoms, nannoliths and grain size distribution. Sedimentary Geology, 282, 40–56. https://doi.org/10.1016/j.sedgeo.2012.07.019

Szczuciński, W., Pawłowska, J., Lejzerowicz, F., Nishimura, Y., Kokociński, M., Majewski, W., Nakamura, Y., Pawlowski, J., 2016. Ancient sedimentary DNA reveals past tsunami deposits. Marine Geology, 381, 29–33. https://doi.org/10.1016/j. margeo.2016.08.00

Switzer, A. D., Felix, R. P., Soria, J. L. A., & Shaw, T. A. (2020). A comparative study of the 2013 typhoon Haiyan overwash sediments from a coastal cave and beach system at Salcedo, Eastern Samar, central Philippines. Marine Geology, 419, 106083. https://doi.org/10.1016/j.margeo.2019.106083

Takada, K., Nakata, T., Miyagi, T., Haraguchi, T. & Nishitani, Y. (2002). Handy Geoslicer—new soil sampler for Quaternary geologist. Chishitsu News, 579, 12-18 (in Japanese).

Takashimizu, Y., Urabe, A., Suzuki, K., & Sato, Y. (2012). Deposition by the 2011 Tohoku-oki tsunami on coastal lowland controlled by beach ridges near Sendai, Japan. Sedimentary Geology, 282, 124–141. https://doi.org/10.1016/j.sedgeo.2012.07.004

Tanioka, Y., Nishimura, Y., Hirakawa, K., Imamura, F., Abe, I., Abe, Y., et al. (2004). Tsunami run-up heights of the 2003 Tokachi-oki earthquake. Earth, Planets and Space, 56(3), 359–365. https://doi.org/10.1186/BF03353065

Tetsuka, H., Goto, K., Ebina, Y., Sugawara, D., & Ishizawa, T. (2020). Historical and geological evidence for the 17th-century tsunami(s) along Kuril and Japan trenches: Implications for the origin of the AD 1611 Keicho earthquake and tsunami, and for the probable future risk potential. Geological Society, London, Special Publications, 501. https://doi.org/10.1144/SP501-2019-60

Watanabe, M., Goto, K., Bricker, J. D., & Imamura, F. (2018). Are inundation limit and maximum extent of sand useful for differentiating tsunamis and storms? An example from sediment transport simulations on the Sendai Plain, Japan. Sedimentary Geology, 364, 204–216. https://doi.org/10.1016/j.sedgeo.2017.12.026

Wessel, P., Smith, W. H. F., Scharroo, R., Luis, J., & Wobbe, F. (2013). Generic Mapping Tools: Improved version released. Eos, Transactions American Geophysical Union, 94(45), 409–410. https://doi.org/10.1002/2013EO450001

Yoshii, T., Tanaka, S., & Matsuyama, M. (2017). Tsunami deposits in a super-large wave flume. Marine Geology, 391, 98–107. https://doi.org/10.1016/j.margeo.2017.07.020

Yokoyama, Y., Miyairi, Y., Aze, T., Yamane, M., Sawada, C., Ando, Y., et al. (2019). A single stage Accelerator Mass Spectrometry at the Atmosphere and Ocean Research Institute, The University of Tokyo. Nuclear Instruments and Methods in Physics Research Section B: Beam Interactions with Materials and Atoms, 455, 311–316. https://doi.org/10.1016/j.nimb.2019.01.055